G-FAST Earthquake Early Warning Potential for Great Earthquakes in Chile

by Brendan W. Crowell, David A. Schmidt, Paul Bodin, John E. Vidale, Ben Baker, Sergio Barrientos, and Jianghui Geng

ABSTRACT

The importance of Global Navigation Satellite System (GNSS)-based earthquake early warning for modeling large earthquakes has been studied extensively over the past decade, and several such systems are currently under development. In the Pacific Northwest, we developed the Geodetic First Approximation of Size and Timing (G-FAST) GNSS-based earthquake early warning module for eventual inclusion in the United States west-coast-wide ShakeAlert system. We also created a test system that allows us to replay past or synthetic earthquakes to help identify problems with both the network architecture and the algorithms. Here, we report on the performance of G-FAST during three large megathrust earthquakes in Chile: the 2010 M_w 8.8 Maule, the 2014 M_w 8.2 Iquique, and the 2015 M_w 8.3 Illapel. Magnitude estimates based on peak ground displacement would be available between 40 and 60 s after the origin time for the three earthquakes, with a magnitude bias less than 0.3 magnitude units. Centroid moment tensor and finite-fault-slip estimates show good agreement with prior results and are available between 60 and 90 s after the origin time. Furthermore, we test the impact of epicentral location errors, latency, and data dropouts on the robustness and timing of alerts and show no significant variability in the results. Finally, we discuss implications for earthquake and tsunami early warning in Chile.

INTRODUCTION

Traditional earthquake early warning (EEW) systems established to date have relied upon seismic data either from strong-motion accelerometers or broadband seismometers. Those systems generally use several seconds of *P*-wave data, either the displacement (P_d) or frequency content (τ_p^{max}, τ_c), to quickly ascertain the magnitude, hypocenter, and origin time (OT) of an event, which in turn is converted to a prediction of ground motion at a location (Allen and Kanamori, 2003; Wu and Zhao, 2006). However, seismic EEW systems tend to suffer magnitude saturation; that is, above a certain magnitude, the magnitude estimate is biased low (Wu *et al.*, 2006; Brown *et al.*, 2011). Global Navigation Satellite System (GNSS) methods do not suffer the problem of magnitude saturation, due to the direct measurement of the ground displacement (Crowell *et al.*, 2013; Melgar *et al.*, 2013). Although GNSS data processed in real time have significantly greater noise than in seismic instruments (1 cm horizontal, 3–5 cm vertical; Genrich and Bock, 2006), it has been shown to reliably capture earthquake ground motions above M_w 6 in the near field (Geng *et al.*, 2013; Melgar, Geng, *et al.*, 2015). Several GNSS-based EEW modules have been proposed for inclusion in the United States west coast ShakeAlert system (Given *et al.*, 2014) under development by the U.S. Geological Survey (USGS), including Geodetic Alarm System (GlarmS; Grapenthin *et al.*, 2014), Bayesian Evidence-based Fault Orientation and Real-Time Earthquake Slip (BEFORES; Minson *et al.*, 2014), and Geodetic First Approximation of Size and Timing (G-FAST;. Crowell *et al.*, 2016). Another algorithm, Real-Time GEONET Analysis System for Rapid Deformation monitoring (REGARD), is being developed in Japan (Kawamoto *et al.*, 2017). GlarmS and BEFORES both use rapidly computed coseismic displacements to obtain a model of fault slip, the details of which vary considerably between the two modules; however, they provide invariably similar products, that is, coseismic slip models. The G-FAST system consists of two modeling modules to rapidly determine earthquake source characteristics. The first module uses the peak ground displacement (PGD) to provide a point-source magnitude estimate (Crowell *et al.*, 2013; Melgar, Crowell, *et al.*, 2015). The second module is a centroid moment tensor (CMT)-driven finite-fault (FF) inversion (Crowell *et al.*, 2012) that uses the coseismic displacements to first invert for a point-source CMT from which two fault planes are created on which to invert for slip. This second module is similar to the BEFORES method except that the orientation of the fault plane is determined with a point-source CMT rather than in a Bayesian framework.

We developed a test system to evaluate the system performance of G-FAST within the ShakeAlert framework. The test system permits us to replay either real or synthetic data and vary key parameters, such as latency, noise, and dropouts. The first test performed was on synthetic data of the 2001 M_w 6.8 Nisqually earthquake in Washington (Crowell *et al.*, 2016). The Nisqually test case was important because it is a fairly common type of event in Puget Sound (roughly 30–50 yr recurrence; Ichinose *et al.*, 2004) and a situation where both seismic and geodetic EEW work well, but is toward the lower

 doi: 10.1785/0220170180

limit of sensitivity for geodetic EEW. In the Nisqually test, it was determined that the PGD module was able to provide a first alert in 17 s after OT, roughly 5 s slower than ElarmS (Kuyuk *et al.*, 2014), with similar magnitude estimates. This updated magnitude from G-FAST would be available 6 s before strong shaking is felt in Seattle. After 30 s, the magnitude and depth estimates from PGD were fully stable for the Nisqually earthquake and close to the final postprocessed estimates (M_w 6.7 and 51 km depth). The CMT-driven FF estimates were available in 38 s after OT and fully stable after 50 s. The FF could not ascertain the correct fault plane, an issue that was seen in other postprocessed studies of the Nisqually earthquake (Ichinose *et al.*, 2004; Kao *et al.*, 2008). In both modeling modules, it was determined that dropouts were the largest source of variability in the model results, indicating that network hardening (i.e., telemetry upgrades) is key for operational early warning.

Because of the lack of historical seismicity in the Cascadia region, it is important to test G-FAST in other subduction zones with sufficient GNSS coverage. Between 2010 and 2016, there have been seven $M_w > 8$ earthquakes across the globe, of which three struck offshore Chile: the 27 February 2010 M_w 8.8 Maule, the 1 April 2014 M_w 8.2 Iquique, and the 16 September 2015 M_w 8.3 Illapel. Subsequent to these events, the Chilean national GNSS network, operated by the Centro Sismológico Nacional (CSN), expanded greatly to over 150 continuous GNSS stations, providing the best recordings of great earthquakes with GNSS outside of Japan. The GNSS station density in Chile is currently comparable with the Cascadia region of the Plate Boundary Observatory.

In this article, we highlight the performance of the G-FAST test system using high-rate (1 Hz) GNSS data from the three recent great earthquakes in Chile, with the end goal of assessing the performance and feasibility of using G-FAST in Chile for earthquake and tsunami early warning. We test several different error conditions (latency, data completeness, and epicentral location uncertainty) to ascertain the robustness of source-parameter estimation over time. The specific source parameters we consider are magnitude, depth, nodal planes, slip azimuth, rake, peak slip values and locations, and final slip models. We also investigate the evolution of source parameters over time and compare our results with previously published results.

G-FAST OVERVIEW AND TEST ENVIRONMENT

G-FAST is an EEW module that uses event triggers from seismic algorithms within ShakeAlert, either single-algorithm based (i.e., ElarmS, Kuyuk *et al.*, 2014; or OnSite, Böse *et al.*, 2009) or the result of the DecisionModule (single event solution based on many algorithms). When an alert is received, modeling is initiated. First, the PGD scaling module determines the magnitude of the event from the peak three-component displacement observed at each station. The PGD module uses a 3 km/s travel-time mask to exclude stations that have not undergone strong shaking yet. Second, the CMT-driven FF inversion runs using the coseismic displacements to determine the fault orientation and slip on the fault. The CMT inversion utilizes the static displacement field Green's functions for a moment tensor in a homogeneous half-space presented by Hashima *et al.* (2008). Using the nodal plane orientations (strike and dip) from the CMT, we create two fault planes with length and width defined by scaling relationships from Wells and Coppersmith (1994), subdivided into 10 along-strike and 5 along-dip segments. Green's functions are defined by Okada's formulation (Okada, 1985), and we use the generalized smoothness equation of Crowell *et al.* (2012) with Laplacian regularization. The coseismic displacements are computed on all stations within a 2–km/s travel-time mask. Both modules are updated every second for up to 5 min, and multiple events can be modeled in parallel. The results of each module are then sent back to the DecisionModule in which an event update would be issued. Note, a next-generation DecisionModule based on ground-motion prediction is being investigated (Minson and Cochran, 2015) to accommodate the finite-source information provided by the geodetic modules.

The G-FAST test system presented by Crowell *et al.* (2016) uses exactly the same modeling core used by the live version, except that the front-end data handling is modified to read data and event messages from files to simulate a real-time environment. The test system allows us to run iterations with simulated conditions to identify weaknesses in the network and the algorithms as well as obtain formal uncertainties. Normally, G-FAST is triggered by XML messages delivered through an ActiveMQ exchange listening to the ShakeAlert DecisionModule. The pertinent information used by G-FAST is the earthquake OT, the epicentral location, the seismically determined magnitude, and a unique event ID. Because there was not an analogous system to ShakeAlert running in Chile at the time, we create an XML message that G-FAST ingests based upon the earliest available USGS National Earthquake Information Center (NEIC) OT and epicentral location. An overview of the individual event parameters is available in Table 1. The CSN implemented rapid source characterization after the Maule earthquake from seismic data that provides information in several minutes; we note the performance for Iquique and Illapel in Table 1. In those events, the CSN locations are 65 and 14 km from the NEIC locations for Iquique and Illapel, respectively, and as more stations have been added, location uncertainties have improved. To take into account expected location uncertainties, we add additional capability into the G-FAST test system, which varies the starting location by up to 20 km in any direction for each iteration. This value roughly matches the expected offshore epicentral uncertainty in ShakeAlert for Cascadia (Hartog *et al.*, 2016).

DATA AND SIMULATIONS

Figure 1 shows all the stations available for each of the three earthquakes. There were 25 GNSS stations available for Maule, 22 for Iquique, and 53 for Illapel (Fig. 1). For Maule, only six

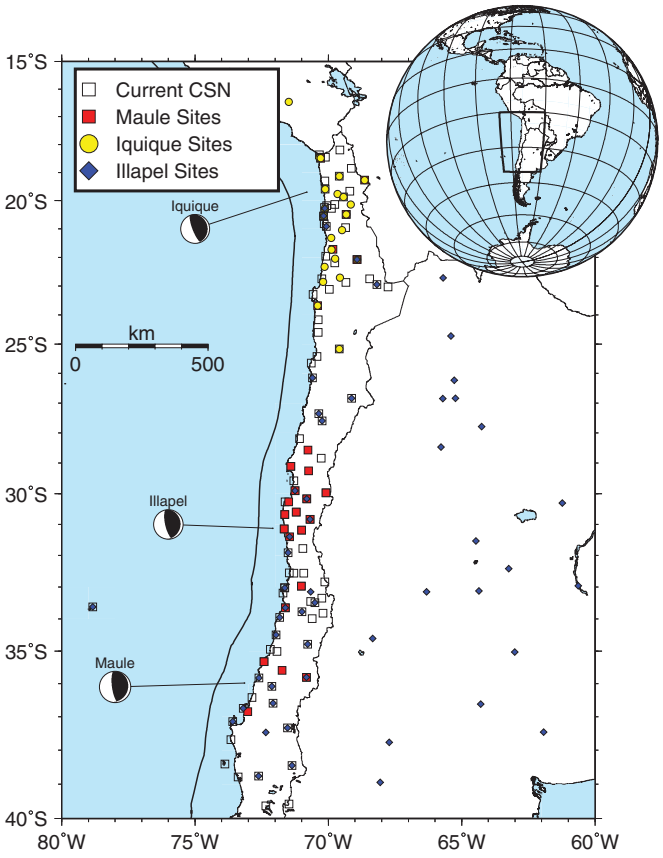

▲ **Figure 1.** Global Navigation Satellite System (GNSS) stations used to model each of the earthquakes. The squares, circles, and diamonds indicate the stations used for the Maule, Iquique, and Illapel earthquakes, respectively. Note that some stations are used for multiple events and have overlapping symbols. The solid line offshore indicates the trench axis from Slab1.0 (Hayes *et al.*, 2012). The unfilled squares show the current state of the Centro Sismológico Nacional (CSN) GNSS network in Chile in 2017.

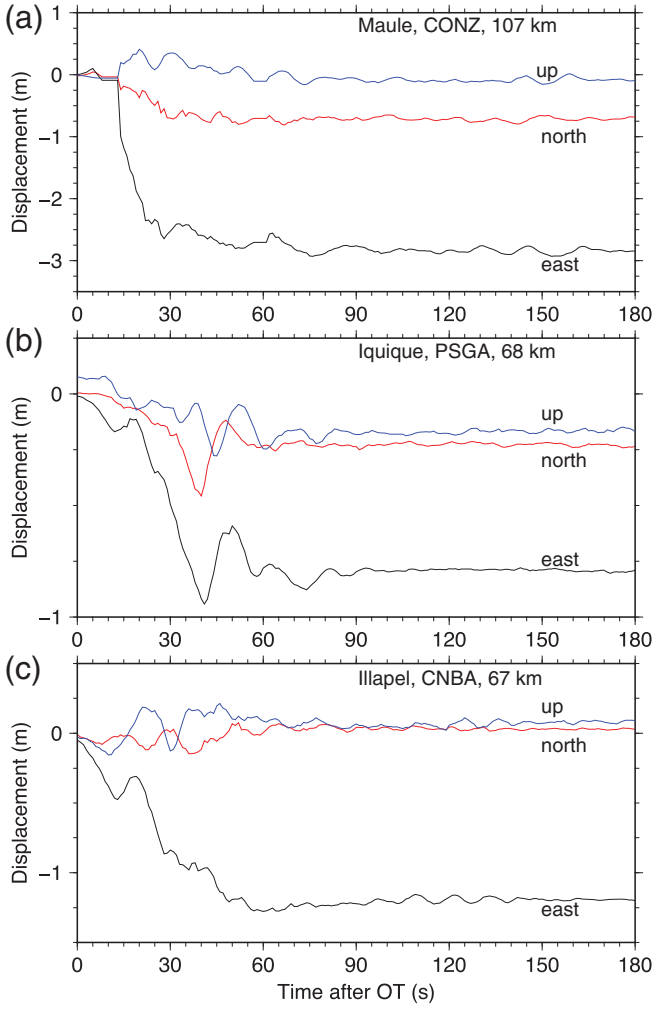

▲ **Figure 2.** Example waveforms for the closest station to each event. GNSS stations are (a) CONZ, 107 km from the Maule epicenter, (b) PSGA, 68 km from the Iquique epicenter, and (c) CNBA, 67 km from the Illapel epicenter. OT, origin time.

Table 1
Overview of Earthquake Parameters

Earthquake	M_w	Latitude (°S)	Longitude (°W)	Depth (km)	Strike/Dip/Rake (°)	Source
Maule	8.8	35.909	72.733	35.0	17/14/108; 178/77/86	NEIC
Maule	8.8	35.980	73.150	23.2	19/18/116; 172/74/82	Global CMT
Iquique	7.8	19.570	70.860	44.0	NA	CSN, 7 min
Iquique	8.2	19.610	70.769	25.0	358/12/107; 161/79/87	NEIC
Iquique	8.1	19.700	70.810	21.6	355/15/106; 159/76/86	Global CMT
Illapel	7.2	31.520	71.810	11.0	NA	CSN, 5 min
Illapel	8.3	31.573	71.674	22.4	353/19/83; 180/71/92	NEIC
Illapel	8.3	31.130	72.090	17.4	7/19/109; 166/72/83	Global CMT

National Earthquake Information Center (NEIC) location is first hypocenter; nodal plane is *W* phase. CMT, Centroid Moment Tensor; CSN, Centro Sismológico Nacional.

stations are less than 500 km away, simply due to the GNSS network installed at the time, which does impact alert timing results presented later. Extensive network densification occurred after Maule, such that 21 of the 22 stations used in this study are within 500 km for the Iquique event 4 yrs later. The GNSS data are processed using the precise point-positioning-with-ambiguity resolution (PPP-AR) method with final International GNSS Service (IGS) orbits (Geng *et al.*, 2013). Using IGS ultra-rapid orbits would result in greater noise levels, but for these earthquakes, the signal-to-noise ratios are large enough that the effects on our results would be minimal (meter level displacements with 1–5 cm level noise). Figure 2 shows the north, east, and up displacement waveforms for the closest stations to each event.

For each earthquake, we run 1000 random realizations of G-FAST using the latency (6 s Poisson distribution), dropout (15% data loss), and location error (20 km epicentral variation) conditions, as well as one simulation with all three error conditions. We do not include the data noise condition into the simulation because the time series are the actual recordings of the earthquakes with noise already included. The data dropout case randomly removes 15% of the data from every waveform, which is well above the standard data loss in real-time GNSS networks; note, there is no temporal or spatial correlations of data dropouts which could exacerbate the impact of dropouts on source estimates. We perform an additional test under ideal conditions using none of the error conditions to obtain a baseline performance. Our final results are reported at 3 min after the OT, although the time when the solutions are stable is much less than this, as noted throughout the Results section.

RESULTS

Table 2 gives an overview of the final parameter estimates at 180 s and their associated uncertainties for the different simulations, as well as the first alert times for the PGD and CMT/FF module. Figure 3 shows the probability density functions (PDFs) of PGD magnitude bias as a function of time after OT for the four simulations. The PDFs show the probability of a simulation solution at each time step; a probability of 1.0 means that all 1000 iterations of the simulation at a specific time had that value. The PDFs of CMT magnitude bias, depth bias, and mean nodal plane bias (difference between main and auxiliary strike/dip/rake) as a function of time are shown in Figure 4 for the simulation under all error conditions. The CMT magnitude, depth, and nodal plane biases are with respect to the final Global CMT parameters (see Table 1). Figure 5 shows the PDFs of the FF results for the simulation under all error conditions. Contained within Figure 5 is the FF magnitude bias, peak slip depth bias (with respect to the Global CMT depth), the weighted average rake, the peak slip, and the location of peak slip at 180 s after OT. In Figures 3–5, the ideal solutions with no error conditions are shown with a solid black line. The final ideal slip model and composite slip model (spatial average of all models) from the simulation with all error conditions are shown in Figures 6–8 for the Maule, Iquique, and Illapel earthquakes, respectively. The composite slip model in Figures 6–8 gives a sense of the overall stability of the FF solutions. The maps are separated into grids (0.5° by 0.5° for Maule and 0.25° by 0.25° for Iquique and Illapel), and a box is filled only if a slip solution existed in the box in any of the 1000 simulations. Each of the boxes is colored by the average of any slip values that exist within the box for all the simulations. Note, if only five simulations had a point on a fault within the box, the sum of the slip is divided by 5 rather than by 1000. The standard deviation of slip for the composite slip models is also shown in Figures 6–8.

Maule

An overview of the PGD simulation results is presented in Table 2, and the PDFs of magnitude bias as a function of time after OT are shown in Figure 3. The first PGD results are available 58 s after OT in the ideal case, with a magnitude of 8.74. This result varies slightly, down to a minimum of M_w 8.64 before settling into a magnitude of 8.68. The latency simulation is the only one that appreciably changes the first alert time, unsurprisingly by 6 s, the same as the mean of the Poisson distribution from which the latency is derived (see Table 2). The location error simulation has a first alert time roughly the same as the ideal case, although with a 2.6 s standard deviation, due to moving the earthquake closer or further away from the first four stations. The four simulations (latency, location error, dropouts, and all three conditions) show very little variability in the PGD magnitude results; however, the location error condition does result in the largest range of magnitude estimates (0.40 magnitude units). Adding latency, as expected, delays the initial magnitude estimate by on average 6 s but has little effect on the magnitude itself. Dropouts show some variability prior to 120 s, with almost none after. This is due to the nature of how offsets are estimated. Early in the earthquake, missing data will impact the estimation of offsets more, leading to higher variability in the solutions. As time goes by, a dropout has less impact on the offset estimation coupled with more data being available, so some missing data will have minimal impact. Table 2 shows the standard deviation of the final magnitude estimates for the four simulations, further demonstrating the importance of the location error condition. As expected, latency and dropouts have standard deviations of 0.01 magnitude units or less, whereas the location error standard deviation has 0.07 magnitude units, close to the 0.08 magnitude units for the simulation with all error conditions.

Figure 4 shows the PDFs of the CMT results for the simulation with all three error conditions. In the ideal case, the CMT results are first available in 82 s after OT, with a magnitude of 8.80, a depth of 35 km, and with nodal planes of 187° and 25°, 81° and 10°, and 87° and 107° for strike, dip, and rake, respectively. The Global CMT nodal plane results are 172° and 19° for strike, 74° and 18° for dip, and 82° and 116° for rake. By 3 min, only six stations are used to compute the CMT, and the results are essentially the same. The simulation shows little variability in the magnitude, depth, and mean nodal plane bias. The CMT depth estimate is biased by roughly 10 km with

Table 2
Overview of Simulation Results

	Initial Alert Time (s)		Final Results (180 s)								
Simulation	PGD	CMT/FF	M_{PGD}	M_{CMT}	M_{FF}	D_{CMT} (km)	NP Bias	D_{FF}^{max} (km)	FF Rake	FF SA	$Slip^{max}$ (m)
	Maule										
Ideal	58	82	8.68	8.80	8.76	35	8.3°	27.7	107.2°	272.0°	14.6
Latency	64.0 ± 2.4	85.3 ± 1.2	8.68 ± 0.00	8.78 ± 0.01	8.78 ± 0.03	28.8 ± 9.5	21.0° ± 19.9°	25.3 ± 4.6	92.0° ± 13.2°	281.5° ± 21.1°	17.1 ± 1.0
Location	58.2 ± 2.6	82.1 ± 3.9	8.68 ± 0.07	8.80 ± 0.01	8.77 ± 0.03	31.9 ± 7.5	14.9° ± 15.7°	27.8 ± 6.8	98.8° ± 12.4°	277.4° ± 16.3°	16.0 ± 1.6
Dropouts	58.0 ± 0.0	82.0 ± 0.0	8.68 ± 0.01	8.80 ± 0.00	8.76 ± 0.01	34.9 ± 1.7	8.6° ± 3.4°	27.7 ± 0.5	106.8° ± 3.1°	272.3° ± 3.5°	14.6 ± 0.4
All	64.3 ± 3.6	85.1 ± 4.2	8.68 ± 0.08	8.79 ± 0.01	8.78 ± 0.04	30.0 ± 9.1	19.6° ± 19.4°	28.7 ± 9.3	94.0° ± 14.4°	280.6° ± 21.5°	16.9 ± 1.5
	Iquique										
Ideal	42	57	8.07	8.32	8.06	34	13.6°	27.2	67.1°	289.6°	5.1
Latency	48.4 ± 1.6	60.5 ± 1.2	8.07 ± 0.00	8.32 ± 0.00	8.07 ± 0.00	35.6 ± 0.6	13.3° ± 0.1°	26.9 ± 0.1	66.0° ± 1.7°	291.3° ± 1.4°	5.3 ± 0.0
Location	41.9 ± 2.2	57.0 ± 3.3	8.07 ± 0.03	8.32 ± 0.01	8.07 ± 0.01	35.7 ± 1.4	13.4° ± 0.4°	27.1 ± 0.3	66.4° ± 3.0°	291.0° ± 2.4°	5.2 ± 0.1
Dropouts	42.0 ± 0.0	57.0 ± 0.0	8.07 ± 0.00	8.33 ± 0.01	8.06 ± 0.01	34.4 ± 0.5	13.6° ± 0.1°	27.2 ± 0.1	67.1° ± 0.4°	289.5° ± 0.4°	5.1 ± 0.0
All	48.0 ± 2.6	60.1 ± 3.3	8.07 ± 0.03	8.32 ± 0.01	8.07 ± 0.01	36.0 ± 1.2	13.4° ± 0.3°	27.1 ± 0.3	64.4° ± 3.2°	292.6° ± 2.5°	5.3 ± 0.1
	Illapel										
Ideal	55	77	8.22	8.33	8.25	46	25.4°	28.1	35.8°	272.4°	7.0
Latency	60.9 ± 2.3	80.2 ± 1.2	8.22 ± 0.00	8.34 ± 0.01	8.18 ± 0.02	43.1 ± 0.9	24.3° ± 0.3°	26.9 ± 0.4	39.5° ± 1.1°	270.9° ± 0.6°	5.8 ± 0.3
Location	54.9 ± 2.1	76.6 ± 3.1	8.22 ± 0.02	8.34 ± 0.03	8.23 ± 0.07	48.9 ± 13.2	26.4° ± 1.5°	33.2 ± 12.1	34.9° ± 5.9°	271.9° ± 2.9°	6.6 ± 0.8
Dropouts	55.0 ± 0.0	77.0 ± 0.0	8.22 ± 0.00	8.34 ± 0.01	8.25 ± 0.01	46.4 ± 0.7	25.5° ± 0.3°	28.5 ± 0.7	35.5° ± 0.5°	272.5° ± 0.3°	7.1 ± 0.1
All	60.7 ± 2.9	79.6 ± 3.4	8.22 ± 0.02	8.35 ± 0.02	8.20 ± 0.05	44.1 ± 6.7	25.4° ± 1.2°	29.4 ± 5.6	38.1° ± 4.0°	271.8° ± 2.0°	6.2 ± 0.7

Uncertainties presented at 1σ level. NP, nodal plane; SA, slip azimuth; D, depth; PGD, peak ground displacement; FF, finite fault.

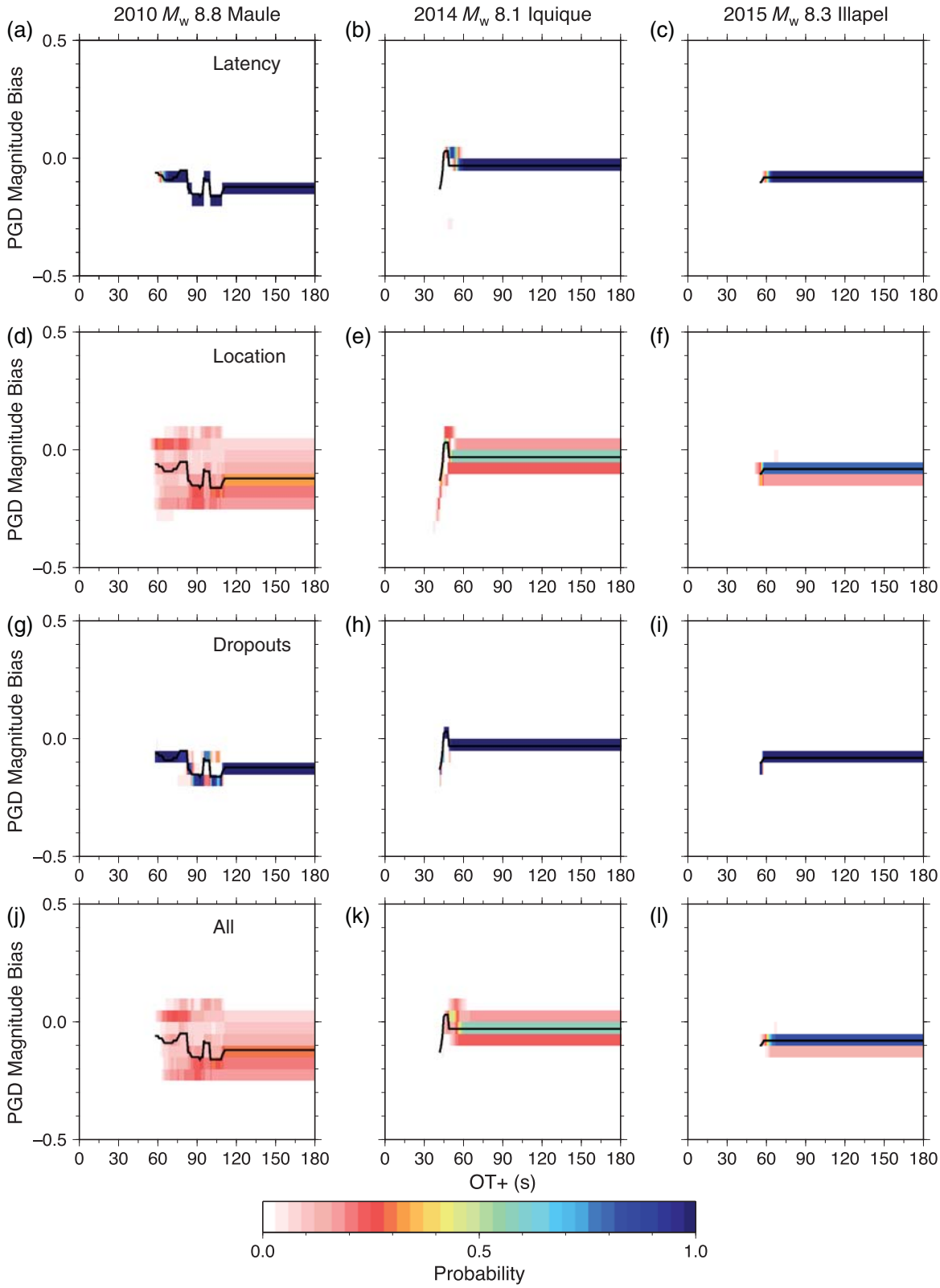

▲ **Figure 3.** Probability density functions (PDFs) of the peak ground displacement (PGD) magnitude bias results as a function of time for the (a,d,g,j) Maule, (b,e,h,k) Iquique, and (c,f,i,l) Illapel earthquakes. The rows, from top to bottom, denote the different simulations: (a–c) latency, (d–f) initial location, (g–i) dropouts, and (j–l) all three error conditions. The ideal results under no error conditions are shown with the solid black line. Magnitude biases are with respect to the Global Centroid Moment Tensor (CMT) values in Table 1.

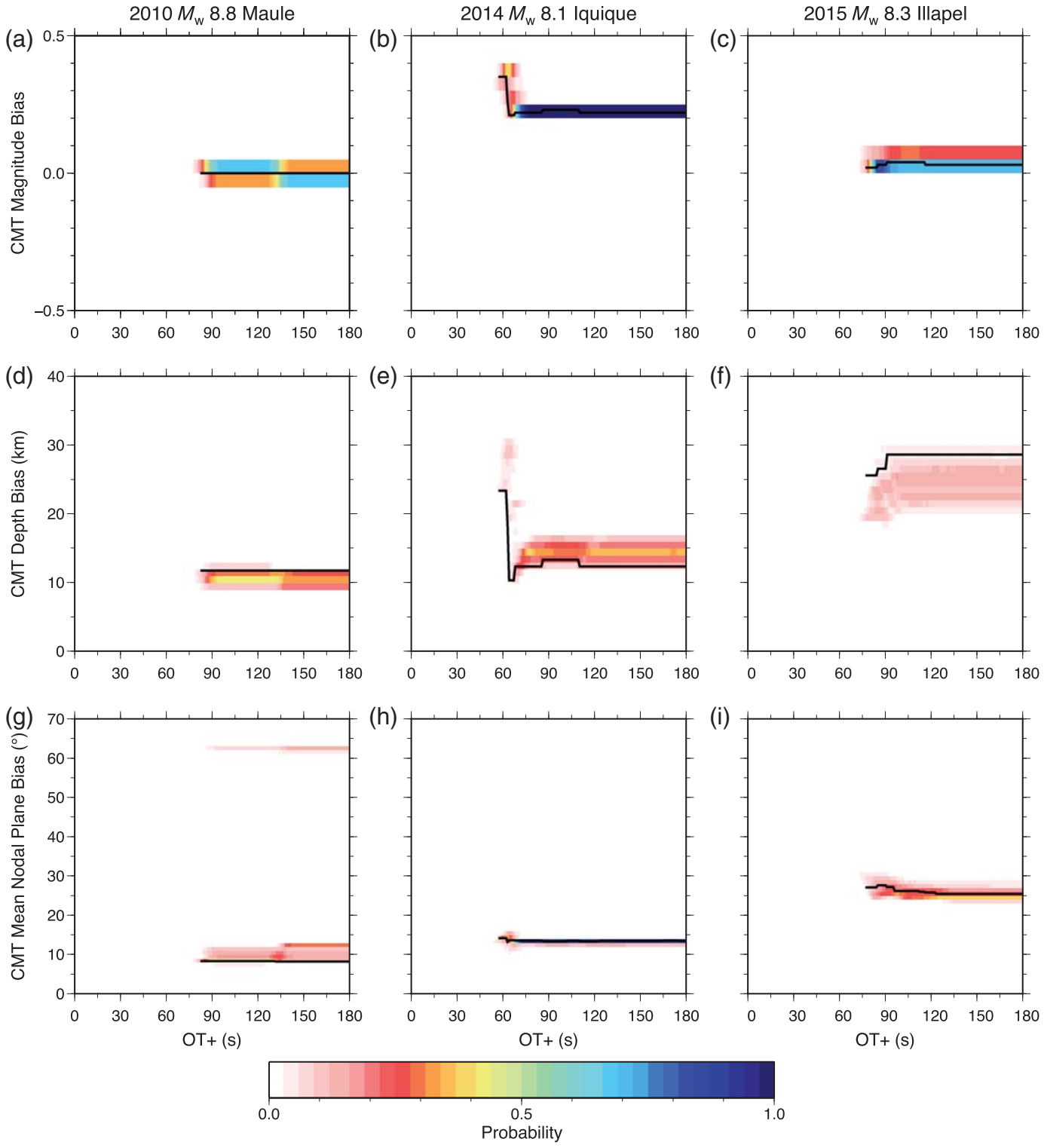

▲ **Figure 4.** PDFs of the CMT results as a function of time for the simulation with all error conditions for the (a,d,g) Maule, (b,e,h) Iquique, and (c,f,i) Illapel earthquakes. The rows, from top to bottom are (a–c) magnitude bias, (d–f) depth bias, and (g–i) mean nodal plane bias, all with respect to the Global CMT values in Table 1. The ideal results under no error conditions are shown with the solid black line.

respect to the Global CMT depth; however, the NEIC hypocenter depth is exactly the same as we find, 35 km.

Figure 5 shows the FF PDFs of magnitude bias, peak slip depth, the weighted average rake, the peak slip along the fault, and the location of peak slip (at 3 min) for the simulation under all error conditions. The first alert times are the same here as the CMT results (because they use the same offsets and offset time criteria). The ideal magnitude starts at

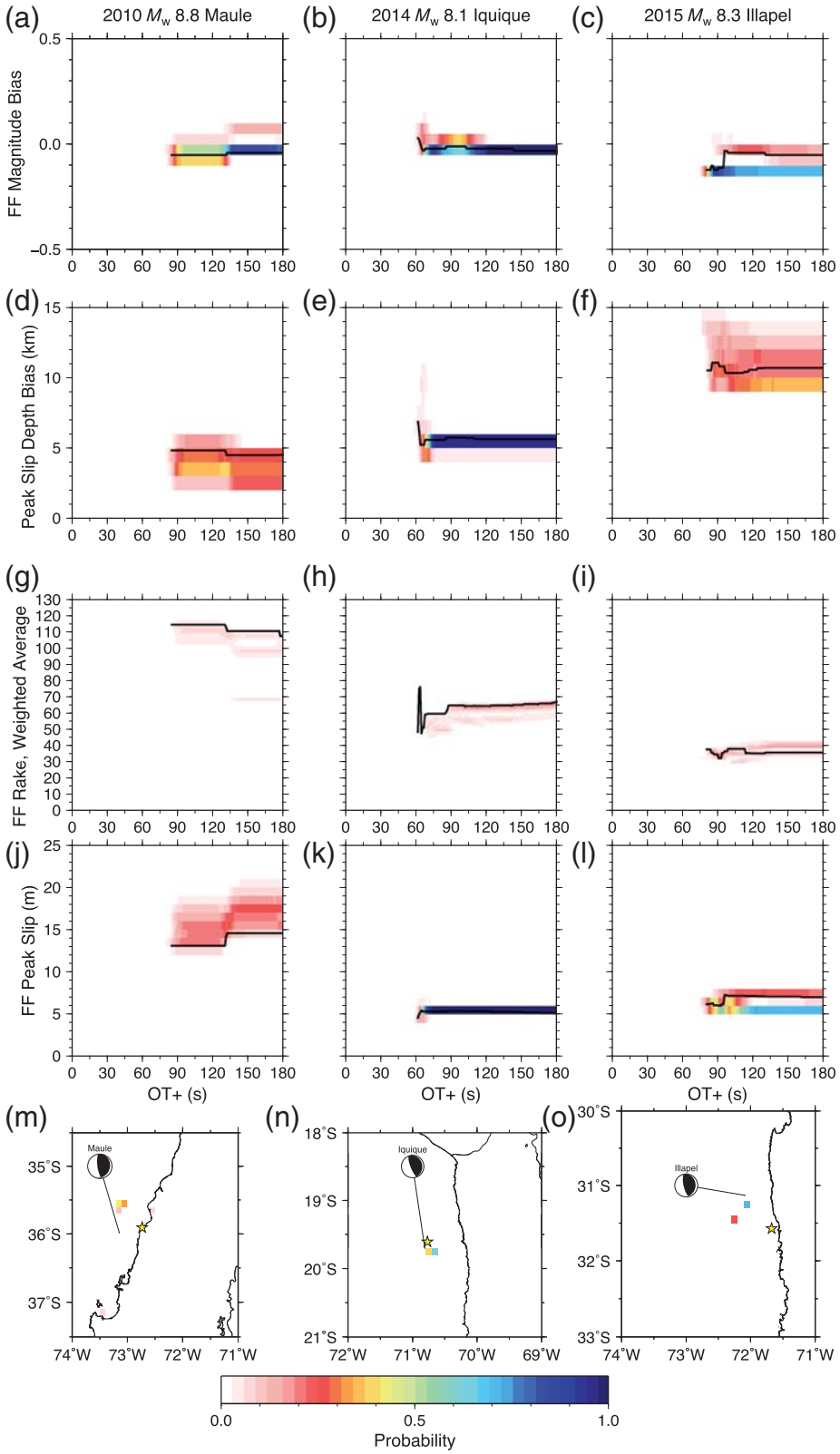

▲ **Figure 5.** PDFs of the finite-fault (FF) results as a function of time for the simulation with all error conditions for the (a,d,g,j,m) Maule, (b, e,h,k,n) Iquique, and (c,f,i,l,o) Illapel earthquakes. The rows, from top to bottom are (a–c) magnitude bias, (d–f) peak slip depth bias, (g–i) weighted average rake, (j–l) peak slip, and (m–o) location of peak slip. Biases are with respect to the Global CMT values in Table 1. The ideal results under no error conditions are shown with the solid black line.

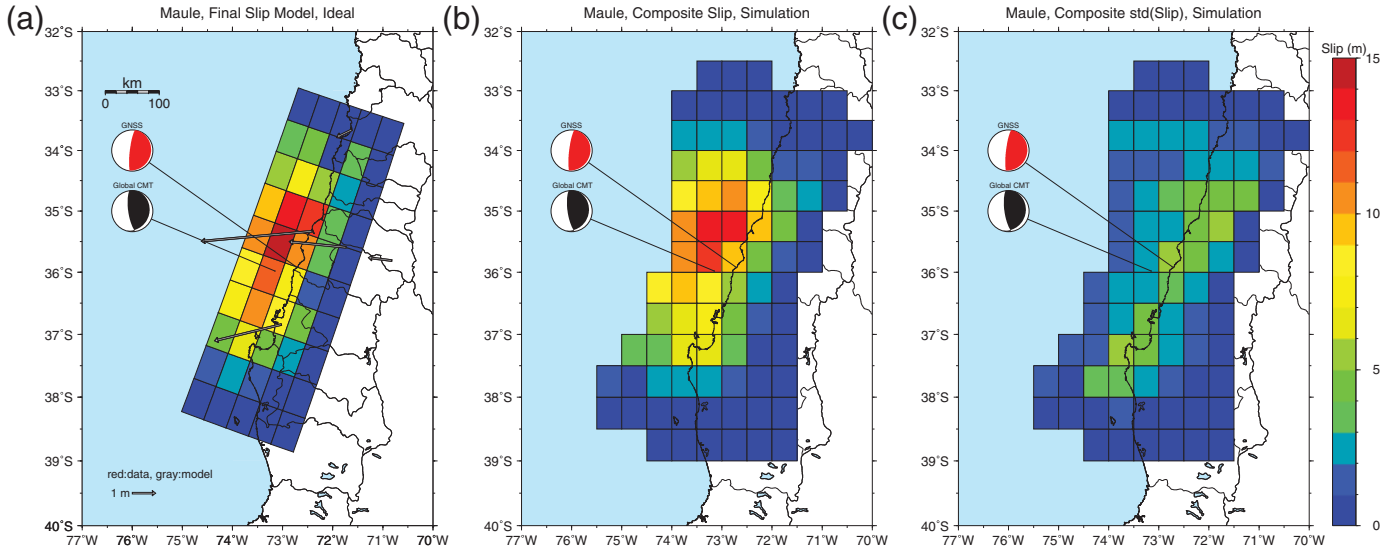

▲ **Figure 6.** The final Maule slip models. The final ideal slip model is shown in (a); the composite mean final slip model under all error conditions is shown in (b); and the standard deviation of slip in the composite slip model under all error conditions in (c). The composite slip model is the average of all 1000 recovered slip models from the simulation with all error conditions. The red focal mechanism plot labeled GNSS is the final ideal CMT.

M_w 8.75 and increases to M_w 8.76, 132 s after OT. The simulation magnitude bias is effectively the same, with a peak range of magnitude biases of 0.15 magnitude units. The peak slip depth is roughly a few kilometers deeper than the Global CMT depth (23.2 km); the simulation range is between 2 and 6 km deeper, with the ideal solution between 4 and 5 km. Delouis *et al.* (2010) find the peak slip location at around 30 km depth, roughly in line with our observation. They also find a peak slip value of about 20 m, which is at the top end of our simulations. The ideal case starts out at 13 m of peak slip and increases to 14.5 m by 3 min. The simulations generally exhibit greater slip, with a range between 14 and 21 m of slip. Given the coarseness and simplicity of our fault grid, having lower levels of peak slip is to be expected because the slip is

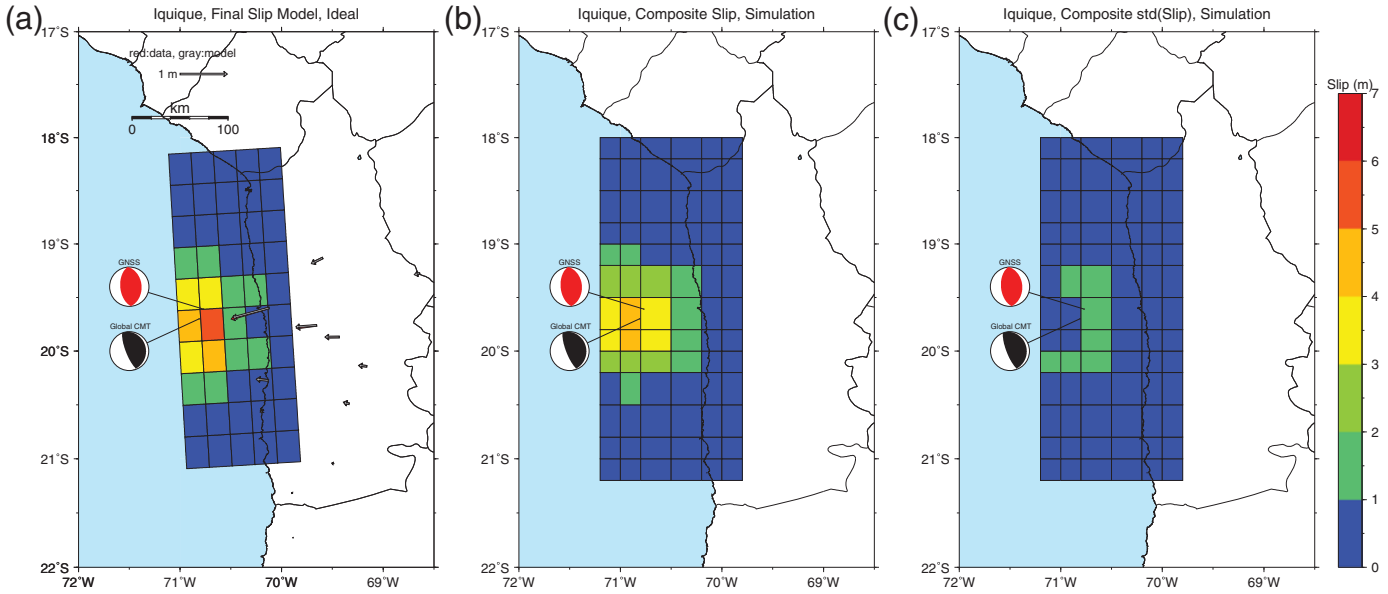

▲ **Figure 7.** The final Iquique slip models. The final ideal slip model is shown in (a); the composite mean final slip model under all error conditions is shown in (b); and the standard deviation of slip in the composite slip model under all error conditions in (c). The composite slip model is the average of all 1000 recovered slip models from the simulation with all error conditions. The red focal mechanism plot labeled GNSS is the final ideal CMT.

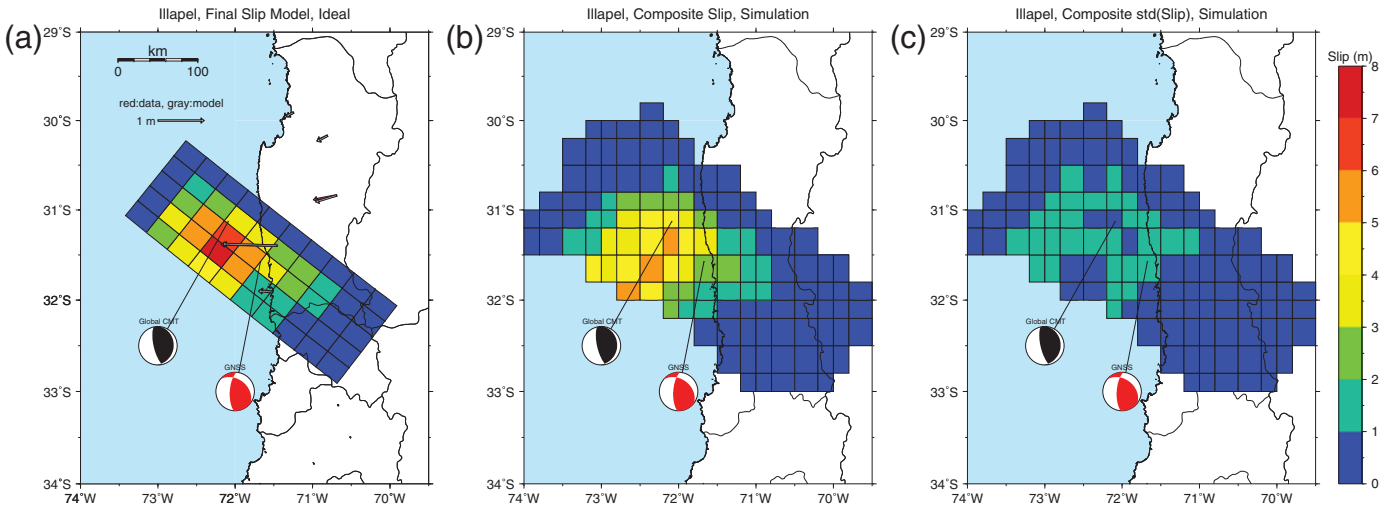

▲ **Figure 8.** The final Illapel slip models. The final ideal slip model is shown in (a); the composite mean final slip model under all error conditions is shown in (b); and the standard deviation of slip in the composite slip model under all error conditions in (c). The composite slip model is the average of all 1000 recovered slip models from the simulation with all error conditions. The red focal mechanism plot labeled GNSS is the final ideal CMT.

spread out over a larger area to conserve moment, although the Maule values are in remarkable agreement with Delouis *et al.* (2010) and Tong *et al.* (2010).

Our weighted average rake (weighted by total slip on a patch) is in line with a mostly dip-slip event, with the ideal solution starting at 115° before settling down to 107°. The simulations tend to be more dip-slip dominated (between 95° and 115°), although a small subset of solutions has a rake of roughly 68°. This small set of solutions with a different rake is due to changing the epicentral location enough that a different set of stations are used because of the travel-time mask.

When looking at the location of peak slip, we see a subset of solutions with peak slip locations roughly 1.5° in latitude further south from the majority of solutions. Because neither the Iquique nor Illapel event displays this behavior, we attribute this effect to the dearth of stations contributing to the Maule solution. The variability in most of the source parameters discussed is also the greatest in the Maule case. Nevertheless, the majority of solutions have a peak slip location around 35.6° S. Both Delouis *et al.* (2010) and Tong *et al.* (2010) show a peak slip location slightly farther north at 35° S.

Figure 6 shows the ideal slip model and the composite slip model (average of all 1000 simulations), indicating that the coarseness of our fault grid can explain some of the bias southward, because each fault patch covers roughly 0.5° along strike. The composite slip model in Figure 6 gives a sense of the overall stability of the FF solutions. The composite slip model has a fairly similar structure to the ideal slip model, and there is very little slip prescribed outside the area of the ideal slip model. Although slip models are inherently nonunique, the fact that the composite slip model behaves similar to the ideal model and has similar structure to previous studies (main slip patch concentrated north of Global CMT location) gives confidence in the robustness of the simulation solutions. The standard deviation of slip in the composite slip model shows that most of the slip variability is near the center of the main slip patch, near the coast.

Iquique

The PGD results for the Iquique earthquake are available earliest of the three events. The first alert in the ideal case is at 42 s after OT, with a magnitude estimate of M_w 7.97 (Fig. 3). In the ideal case, there is some variability (0.16 magnitude units) for 6 s before the magnitude settles into M_w 8.07 for the remainder of the 3 min, right in line with the Global CMT magnitude of M_w 8.1. As with Maule, the simulation with the location error condition bears the most similarity to the simulation under all error conditions; the latency and dropout conditions only cause variability in the first 5–10 s. The total range of magnitude estimates for the simulation with all error conditions at all times is 0.48 magnitude units; the standard deviation, however, is much tighter at 0.03 magnitude units.

The initial ideal CMT nodal planes are 330° and 163° for strike, 36° and 55° for dip, and 80° and 97° for rake, available in 57 s after OT. The Global CMT nodal plane results are 355° and 159° for strike, 15° and 76° for dip, and 106° and 86° for rake, which is roughly a 15° average nodal plane bias. At 63 s after OT, the ideal nodal plane results converge to 355° and 175° for strike, 52° and 38° for dip, and 90° and 90° for rake where they stay within a degree for the remainder of the simulation. The initial ideal depth estimate is 45 km with a magnitude of 8.45. This higher bias persists until 63 s after OT, at which it converges to the final answer of 34 km depth and a magnitude 8.32. Both the depth and magnitude are biased with respect to the NEIC and Global CMT values by roughly 9–12 km and 0.12–0.22 magnitude units.

The FF results have a similar variability to the CMT results between 57 and 63 s after OT and then converge to the final results for magnitude, peak slip depth, rake, and peak slip

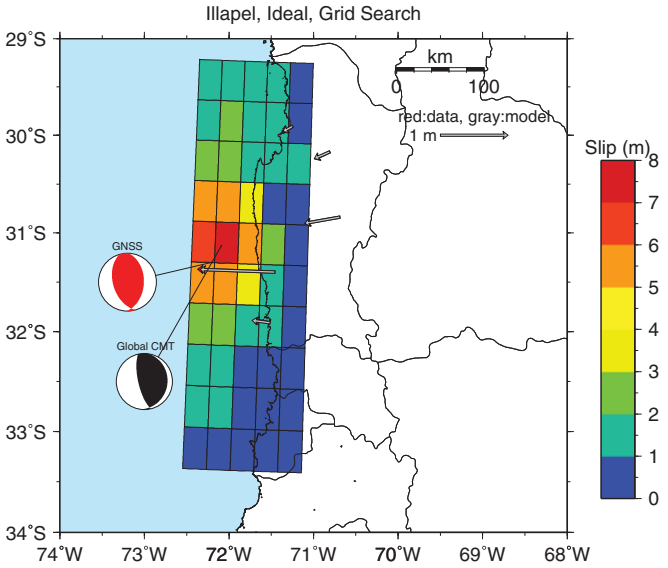

▲ **Figure 9.** The final Illapel slip model after performing a full grid search for centroid location. The red focal mechanism plot labeled GNSS is the final ideal CMT after the grid search.

(Fig. 5). Once the FF results stabilize, none of the source estimates present much variability, further evidenced by the simplicity of the composite slip model and the standard deviation of slip in Figure 7. Most studies of the Iquique earthquake place a rather compact slip distribution just south of the hypocenter, with peak slips ranging from 5 to 7 m and a main slip patch roughly 150 km by 150 km (An *et al.*, 2014; Hayes *et al.*, 2014; Yagi *et al.*, 2014). Our solution is in line with these results, with a peak slip just above 5 m, a slip azimuth and rake angle indicating slip slightly north of west, and a peak slip depth of 27 km. The simulation with epicentral location errors provides the greatest variability; however, all FF source estimates exhibit very low variability.

Illapel

The Illapel PGD results (Fig. 3) show the smallest amount of variation of any of the events, with a first alert at 55 s and the magnitude estimate varying by less than 0.05 magnitude units for the remainder of the event for the ideal case. The magnitude is slightly low by less than 0.1 magnitude unit. The location error simulation causes the most variability but it is essentially negligible, with a total magnitude range of 0.1 magnitude units and standard deviation of 0.02 magnitude units.

The CMT results tell a very different story than the PGD results (Fig. 4). The magnitude variation is roughly the same as the PGD case, but there are significant biases in both the source depth and mean nodal plane bias. The initial CMT magnitude estimate is available in 77 s in the ideal case, with a magnitude of 8.32, a depth of 43 km, and with nodal planes of 311° and 189°, 39° and 67°, and 38° and 123° for strike, dip, and rake, respectively. The Global CMT nodal plane results are 7° and 166° for strike, 19° and 72° for dip, and 109° and 83° for rake. The source estimates vary little for the remainder of the ideal simulation. The final source depth is significantly biased by about 28 km, and the mean nodal plane bias is 25.4° in the ideal case (see Table 2). We attribute these biases to the large distance between the epicenter and centroid locations, which is roughly 63 km. Of note however, the initial slip azimuths (strike minus rake) are 272° and 67° compared with the Global CMT values of 258° and 83°, indicating that the GNSS displacements are guiding the inverted deformation pattern appropriately. For the simulations, the most appreciable variability is in the depth estimate, dominated by the epicentral location error. The simulation with all error conditions has a depth standard deviation of 6.7 km, which is smaller than considering epicentral location errors alone (13.2 km) due to a smoothing effect of removing data from the simulation. The magnitude estimates all have a standard deviation less than 0.03 magnitude units for all simulations and the nodal plane bias varies by only about a degree even though it is biased heavily.

The FF results behave similar to the CMT results. The initial ideal magnitude is slightly low at 8.18 and gradually increases to a final magnitude of 8.25. The peak slip depth is also biased deeper by roughly 11 km, with a weighted average rake of 37°. The initial peak slip is 6.2 m and increases to a final value of 7.0 m. Previous studies found peak slip values between 5 and 10 m (Heidarzadeh *et al.*, 2016; Melgar, Fan, *et al.*, 2016; Tilmann *et al.*, 2016; Ye *et al.*, 2016). The location of peak slip in the simulation with all error conditions (Fig. 5) is just south of the Global CMT location, between 31.25° S and 31.5° S. Our final ideal slip model (Fig. 8) is roughly in line with backprojection results from Ye *et al.* (2016); however, the results from Heidarzadeh *et al.* (2016) and Tilmann *et al.* (2016) have their main fault patches slightly north of 31° S. The Melgar, Allen, *et al.* (2016) source model using several datasets and methods including GPS, strong motion, tide gauge, and teleseismic backprojection have a major fault patch in line with ours south of 31° S, as well as one north of 31° S, in line with Heidarzadeh *et al.* (2016) and Tilmann *et al.* (2016). The composite slip model (Fig. 8) for the simulation with all error conditions shows greater variability than the Iquique or Maule earthquake. As with the CMT, we see a considerable rotation of the fault plane; however, the slip azimuth is roughly due west at 272° (Table 2). The standard deviation of slip in the composite slip model shows all the variability in the offshore region near the main slip patch.

Addition of Grid Search for CMT and PGD Modules

Although the nodal plane results for Maule and Iquique were close to the Global CMT values, the values for Illapel were highly rotated due to the large discrepancy between the epicenter and centroid locations. To this end, we added additional capabilities into G-FAST for a full grid search for both the CMT and PGD modules. For the grid search, we minimize the L1 norm of the residual displacements (predicted minus actual displacements). The grid size is customizable, but for the purposes here, we search in 1° in all directions at 0.05° grid spacing, at 1 km in depth increments. Figure 9 shows the final ideal CMT and FF results for the Illapel earthquake with the grid

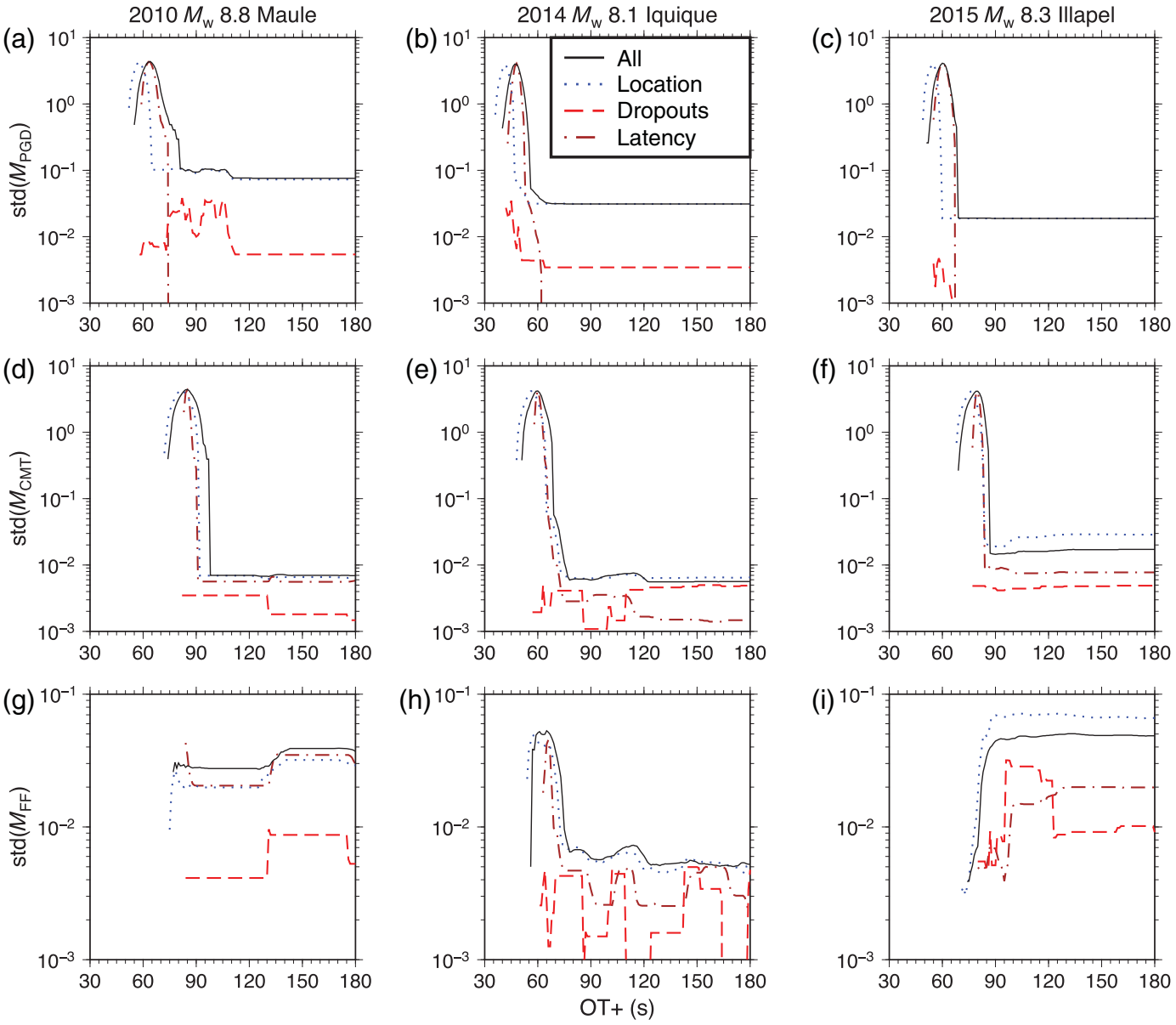

▲ **Figure 10.** Standard deviation of magnitude estimates from the different simulations for (a–c) PGD, (d–f) CMT, and (g–i) FF as a function of time for the (a,d,g) Maule, (b,e,h) Iquique, and (c,f,i) Illapel earthquakes. Notice the difference in scale for the FF.

search enabled. The new CMT location is 31.30° S, 72.19° W, and 32 km deep, with magnitude predictions of 8.58 and 8.50 for the CMT and FF, respectively. The nodal planes are much more consistent with the Global CMT results, with 2.26° and 163.43° for strike, 42.94° and 48.62° for dip, and 104.02° and 77.29° for rake. The final slip model has a peak slip of 8.0 m. The location of peak slip shifts northward slightly (see Fig. 9 vs. Fig. 8), roughly centered on the Global CMT location, more in line with previous studies. The addition of the grid search in these examples is also computationally fast; in the C version of G-FAST for the Illapel case, the CMT grid search is capable of running each epoch (here 1 s) in well under 1 s. The speed of the grid search will depend on the number of stations and the number of grid points, but we are confident that it will remain computationally expedient in the future when considering more stations.

Simulation Variance

In the Results section, we discussed briefly the results of all four simulations; however, much of the discussion was focused on the simulation using all three error conditions. It is useful, however, to look more carefully at the variability of the different simulations as a function of time. Figure 10 shows the standard deviation of magnitude estimates for the different simulation conditions: latency, location error, dropouts, and all three conditions. The effects of the different simulations is significantly different for PGD scaling than for the CMT/FF inversion; however, they all follow similar patterns.

For PGD scaling, the effects of dropouts is at least an order of magnitude less than any of the other simulations throughout the whole time history of the simulations. The latency simulation mimics the curve of the simulation with all error conditions for the first 10–20 s before dropping off toward insignificance. The epicentral location-error simulation follows the simulation with all error conditions closely for all three earthquakes, indicating that the impact of location errors is the most significant. The final standard deviation of magnitude for PGD scaling is 0.08, 0.03, and 0.02 magnitude units for the Maule, Iquique, and Illapel earthquakes, respectively, and the results drop below 0.1 magnitude units at 84, 56, and 69 s after OT.

The interplay between the three error conditions is very different when using the coseismic displacements for the CMT/FF inversion. The latency and location simulations now both follow closely the simulation with all error conditions. The impact of latency here is surprising; however, with so few stations contributing toward the solutions here, latency can have an impact over a much longer time span due to removing or adding a specific station to the solution at different times. Dropouts have the biggest impact on the Iquique earthquake, with an almost equivalent importance to location uncertainty. Most surprising is that the impact of location errors for the Illapel earthquake is greater than the simulation with all error conditions. This would indicate that removing data or altering the order of data flow would calm the effect of location errors due to the already large distance between the hypocenter and centroid for the Illapel earthquake.

DISCUSSION AND CONCLUSIONS

The PGD module works well in modeling the magnitude of all three earthquakes without modification and using the Crowell *et al.* (2016) regression coefficients. The CMT/FF module, however, requires the addition of a full CMT grid search to minimize orientation biases of the fault planes in the event in which the hypocenter and centroid are significantly far apart; this was the case for the Illapel earthquake. Nonetheless, while the orientation of the fault plane was biased for Illapel, the rake angle in both the CMT and FF compensates to align the slip azimuth with the true rake, minimizing the impacts of the orientation bias. This is still a serious issue with regard to ground-motion prediction and, to a lesser extent, tsunami prediction. For ground-motion prediction, the minimum distance to the surface projection of the slip surface, the Joyner–Boore distance (e.g., Boore *et al.*, 1997), and the minimum distance to the rupture plane have the greatest impacts on strong ground motion outside of site effects. A rotation of the rupture plane will impact both of these distance measures and cause an overestimation of ground motion where the fault is rotated toward land (the southern part of the fault surface in Fig. 8) and an underestimation in ground motion where the fault is rotated away from land (the northern part of the fault in Fig. 8). Although it is difficult to assess the true impacts toward ground-motion prediction because it is highly dependent on a number of factors (epicenter, centroid, slip model, orientation biases, depth biases, local geology, etc.), we recognize that minimizing any biases in the inverted slip model will help ameliorate biases in the ground-motion prediction. Moreover, with near-field tsunami prediction, a good model of seafloor deformation is required, which is still possible given fault-plane orientation biases, as long as the slip azimuth is correct. Nonetheless, Melgar, Allen, *et al.* (2016) showed that, using a very simple source model derived from PGD magnitudes, one could obtain a near-field tsunami warning map (at the prefecture or county level) with minimal errors. With more complex rupture models based on a FF inversion or a kinematic inversion, a more granular view of tsunami inundation is possible, all within a matter of minutes.

We have shown given the current network of GNSS stations in Chile, unsaturated real-time source models of great earthquakes would be available and stable within a few minutes. The PGD, CMT, and FF models are all robust against common network-wide error conditions, such as latency, data completeness, and epicentral location uncertainty. Good slip models (with rake angles in line with the true slip azimuth) can still be obtained with long ruptures or ruptures where the hypocenter is far from the centroid, although we added grid searching capabilities to G-FAST to minimize any orientation biases that may arise. These models have the potential to provide coastal communities in Chile with extra warning time of impending strong shaking and tsunami inundation with direct implications for human and financial loss reduction.

DATA AND RESOURCES

The raw Global Navigation Satellite System (GNSS) data used in this study are publically available at http://www.sismologia.cl/ (last accessed May 2017). Processed displacement waveforms are available upon request to the corresponding author in Seismic Analysis Code (SAC) format and were created by Jianghui Geng, Wuhan University, and Diego Melgar, University of California Berkeley. Global Centroid Moment Tensor (CMT) information is available at http://www.globalcmt.org/CMTsearch.html (last accessed May 2017). We utilized the following U.S. Geological Survey (USGS) National Earthquake Information Center (NEIC) event pages for the information presented in Table 1: Maule, https://web.archive.org/web/20100301114502/http://earthquake.usgs.gov:80/earthquakes/eqinthenews/2010/us2010tfan/; Iquique, https://earthquake.usgs.gov/earthquakes/eventpage/usc000nzvd#executive; and Illapel, https://earthquake.usgs.gov/earthquakes/eventpage/us20003k7a#executive (all last accessed May 2017).

ACKNOWLEDGMENTS

The authors would like to thank the two anonymous reviewers for helpful comments that improved the article. Work at the University of Washington was funded by the Gordon and Betty Moore Foundation (Grant Number 663450) and the Amazon Catalyst program.

REFERENCES

Allen, R. M., and H. Kanamori (2003). The potential for earthquake early warning in southern California, *Science* **300,** 786–789, doi: 10.1126/science.1080912.

An, C., I. Sepúlveda, and P. L.-F. Liu (2014). Tsunami source and its validation of the 2014 Iquique, Chile, earthquake, *Geophys. Res. Lett.* **41,** no. 11, 3988–3994, doi: 10.1002/2014GL060567.

Boore, D. M., W. B. Joyner, and T. E. Fumal (1997). Equations for estimating horizontal response spectra and peak acceleration from western North American earthquakes: A summary of recent work, *Seismol. Res. Lett.* **68,** no. 1, 128–153.

Böse, M., E. Hauksson, K. Solanki, H. Kanamori, Y.-M. Wu, and T. Heaton (2009). A new trigger criterion for improved real-time performance of onsite earthquake early warning in southern California, *Bull. Seismol. Soc. Am.* **99,** no. 2A, 897–905, doi: 10.1785/0120080034.

Brown, H. M., R. M. Allen, M. Hellweg, O. Khainovski, D. Neuhauser, and A. Souf (2011). Development of the ElarmS methodology for earthquake early warning: Realtime application in California and offline testing in Japan, *Soil Dynam. Earthq. Eng.* **31,** 188–200, doi: 10.1016/j.soildyn.2010.03.008.

Crowell, B. W., Y. Bock, and D. Melgar (2012). Real-time inversion of GPS data for finite fault modeling and rapid hazard assessment, *Geophys. Res. Lett.* **39,** L09305, doi: 10.1029/2012GL051318.

Crowell, B. W., D. Melgar, Y. Bock, J. S. Haase, and J. Geng (2013). Earthquake magnitude scaling using seismogeodetic data, *Geophys. Res. Lett.* **40,** 6089–6094, doi: 10.1002/2013GL058391.

Crowell, B. W., D. A. Schmidt, P. Bodin, J. E. Vidale, J. Gomberg, J. R. Hartog, V. C. Kress, T. I. Melbourne, M. Santillan, S. E. Minson, *et al.* (2016). Demonstration of the Cascadia G-FAST geodetic earthquake early warning system for the Nisqually, Washington, earthquake, *Seismol. Res. Lett.* **87,** doi: 10.1785/0220150255.

Delouis, B., J.-M. Nocquet, and M. Vallée (2010). Slip distribution of the February 27, 2010 $M_w = 8.8$ Maule earthquake, central Chile, from static and high-rate GPS, InSAR, and broadband teleseismic data, *Geophys. Res. Lett.* **37,** L17305, doi: 10.1029/2010GL043899.

Geng, J., Y. Bock, D. Melgar, B. W. Crowell, and J. S. Haase (2013). A new seismogeodetic approach applied to GPS and accelerometer observations of the 2012 Brawley seismic swarm: Implications for earthquake early warning, *Geochem. Geophys. Geosys.* **14,** 2124–2142, doi: 10.1002/ggge.20144.

Genrich, J. F., and Y. Bock (2006). Instantaneous geodetic positioning with 10–50 Hz GPS measurements: Noise characteristics and implications for monitoring networks, *J. Geophys. Res.* **111,** no. B03403, doi: 10.1029/2005JB003617.

Given, D. D., E. S. Cochran, T. Heaton, E. Hauksson, R. Allen, P. Hellweg, J. Vidale, and P. Bodin (2014). Technical implementation plan for the ShakeAlert production system: An earthquake early warning system for the west coast of the United States, *U.S. Geol. Surv. Open-File Rept. 2014-1097*, 25 p., doi: 10.3133/ofr20141097.

Grapenthin, R., I. A. Johanson, and R. M. Allen (2014). Operational real-time GPS-enhanced earthquake early warning, *J. Geophys. Res.* **119,** 7944–7965, doi: 10.1002/2014JB011400.

Hartog, J. R., V. C. Kress, S. D. Malone, P. Bodin, J. E. Vidale, and B. W. Crowell (2016). Earthquake early warning: ShakeAlert in the Pacific Northwest, *Bull. Seismol. Soc. Am.* **106,** 1875–1886, doi: 10.1785/0120150261.

Hashima, A., Y. Takada, Y. Fukahata, and M. Matsu'ura (2008). General expressions for internal deformation due to a moment tensor in an elastic/viscoelastic multilayered half-space, *Geophys. J. Int.* **175,** 992–1012, doi: 10.1111/j.1365-246X.2008.03837.x.

Hayes, G. P., M. W. Herman, W. D. Barnhart, K. P. Furlong, S. Riquelme, H. M. Benz, E. Bergman, S. Barrientos, P. S. Earle, and S. Samsonov (2014). Continuing megathrust earthquake potential in Chile after the 2014 Iquique earthquake, *Nature* **512,** no. 7514, 295–298, doi: 10.1038/nature13677.

Hayes, G. P., D. J. Wald, and R. L. Johnson (2012). Slab1.0: A three-dimensional model of global subduction zone geometries, *J. Geophys. Res.* **117,** no. B01302, doi: 10.1029/2011JB008524.

Heidarzadeh, M., S. Murotani, K. Satake, T. Ishibe, and A. R. Gusman (2016). Source model of the 16 September 2015 Illapel, Chile, M_w 8.4 earthquake based on teleseismic and tsunami data, *Geophys. Res. Lett.* **43,** no. 2, 643–650, doi: 10.1002/2015GL067297.

Ichinose, G. A., H. K. Thio, and P. G. Somerville (2004). Rupture process and near-source shaking of the 1965 Seattle-Tacoma and 2001 Nisqually, intraslab earthquakes, *Geophys. Res. Lett.* **31,** L10604, doi: 10.1029/2004GL019668.

Kao, H., K. Wang, R.-Y. Chen, I. Wada, J. He, and S. D. Malone (2008). Identifying the rupture place of the 2001 Nisqually, Washington, earthquake, *Bull. Seismol. Soc. Am.* **98,** 1546–1558, doi: 10.1785/0120070160.

Kawamoto, S., Y. Ohta, Y. Hiyama, M. Todoriki, T. Nishimura, T. Furuya, Y. Sato, T. Yahagi, and K. Miyagawa (2017). REGARD: A new GNSS-based real-time finite fault modeling system for GEONET, *J. Geophys. Res.* **122,** doi: 10.1002/2016JB013485.

Kuyuk, H. S., R. M. Allen, H. Brown, M. Hellweg, I. Henson, and D. Neuhauser (2014). Designing a network-based earthquake early warning algorithm for California: ElarmS-2, *Bull. Seismol. Soc. Am.* **104,** 162–173, doi: 10.1785/0120130146.

Melgar, D., R. M. Allen, S. Riquelme, J. Geng, F. Bravo, J. C. Baez, H. Parra, S. Barrientos, P. Fang, Y. Bock, *et al.* (2016). Local tsunami warnings: Perspectives from recent large events, *Geophys. Res. Lett.* **43,** no. 3, 1109–1117, doi: 10.1002/2015GL067100.

Melgar, D., Y. Bock, D. Sanchez, and B. W. Crowell (2013). On robust and reliable automated baseline corrections for strong motion seismology, *J. Geophys. Res.* **118,** 1177–1187, doi: 10.1002/jgrb.50135.

Melgar, D., B. W. Crowell, J. Geng, R. M. Allen, Y. Bock, S. Riquelme, E. M. Hill, M. Protti, and A. Ganas (2015). Earthquake magnitude calculation without saturation from the scaling of peak ground displacement, *Geophys. Res. Lett.* **42,** 5197–5205, doi: 10.1002/2015GL064278.

Melgar, D., W. Fan, S. Riquelme, J. Geng, C. Liang, M. Fuentes, G. Vargas, R. M. Allen, P. M. Shearer, and E. J. Fielding (2016). Slip segmentation and slow rupture to the trench during the 2015, M_w 8.3 Illapel, Chile earthquake, *Geophys. Res. Lett.* **43,** no. 3, 961–966, doi: 10.1002/2015GL067369.

Melgar, D., J. Geng, B. W. Crowell, J. S. Haase, Y. Bock, W. C. Hammond, and R. M. Allen (2015). Seismogeodesy of the 2014 M_w 6.1 Napa earthquake, California: Rapid response and modeling of fast rupture on a dipping strike-slip fault, *J. Geophys. Res.* **120,** no. 7, 5013–5033, doi: 10.1002/2015JB011921.

Minson, S. E., and E. S. Cochran (2015). Combining multiple rupture models in real-time for earthquake early warning, presented at *2015 Fall Meeting AGU*, San Francisco, California, 14–18 December, Abstract S22B-06.

Minson, S. E., J. R. Murray, J. O. Langbein, and J. S. Gomberg (2014). Real-time inversions for finite fault slip models and rupture geometry based on high-rate GPS data, *J. Geophys. Res.* **119,** 3201–3231, doi: 10.1002/2013JB010622.

Okada, Y. (1985). Surface deformation due to shear and tensile faults in a half-space, *Bull. Seismol. Soc. Am.* **75,** 1135–1154.

Tilmann, F., Y. Zhang, M. Moreno, J. Saul, F. Eckelmann, M. Palo, Z. Deng, A. Babeyko, K. Chen, J. C. Baez, *et al.* (2016). The 2015 Illapel earthquake, central Chile: A type case for a characteristic earthquake? *Geophys. Res. Lett.* **43,** no. 2, 574–583, doi: 10.1002/2015GL066963.

Tong, X., D. Sandwell, K. Luttrell, B. Brooks, M. Bevis, M. Shimada, J. Foster, R. Smalley, H. Parra, J. C. Báez Soto, *et al.* (2010). The 2010 Maule, Chile earthquake: Downdip rupture limit revealed by space geodesy, *Geophys. Res. Lett.* **37,** no. 24, L24311, doi: 10.1029/2010GL045805.

Wells, D. L., and K. J. Coppersmith (1994). New empirical relationships among magnitude, rupture length, rupture width, rupture area, and surface displacement, *Bull. Seismol. Soc. Am.* **84,** 974–1002.

Wu, Y.-M., and L. Zhao (2006). Magnitude estimation using the first three seconds *P*-wave amplitude in earthquake early warning, *Geophys. Res. Lett.* **33,** L16312, doi: 10.1029/2006GL026871.

Wu, Y.-M., H.-Y. Yen, L. Zhao, B.-S. Huang, and W.-T. Liang (2006). Magnitude determination using initial *P* waves: A single-station approach, *Geophys. Res. Lett.* **33,** L05306, doi: 10.1029/2005GL025395.

Yagi, Y., R. Okuwaki, B. Enescu, S. Hirano, Y. Yamagami, S. Endo, and T. Komoro (2014). Rupture process of the 2014 Iquique Chile earthquake in relation with the foreshock activity, *Geophys. Res. Lett.* **41,** no. 12, 4201–4206, doi: 10.1002/2014GL060274.

Ye, L., T. Lay, H. Kanamori, and K. D. Koper (2016). Rapidly estimated seismic source parameters for the 16 September 2015 Illapel, Chile M_w 8.3 earthquake, *Pure Appl. Geophys.* **173,** no. 2, 321–332, doi: 10.1007/s00024-015-1202-y.

Brendan W. Crowell
David A. Schmidt
Paul Bodin
John E. Vidale[1]
Department of Earth and Space Sciences
University of Washington
Johnson Hall Rm-070, Box 351310
4000 15th Avenue NE
Seattle, Washington 98195-1310 U.S.A.
crowellb@uw.edu

Ben Baker
Instrumental Software Technologies, Inc.
77 Van Dam Street, Suite 9
Saratoga Springs, New York 12866 U.S.A.

Sergio Barrientos
Centro Sismológico Nacional
Universidad de Chile
Blanco Encalada 2002
Casilla 2777
Santiago, Chile

Jianghui Geng
GNSS Research Center
Wuhan University
129 Luoyu Road
Wuchang District
Wuhan 430079, China

Published Online 7 February 2018

[1] Now at Department of Earth Sciences, University of Southern California, Los Angeles, California U.S.A.